Journal of Materials Chemistry B

ROYAL SOCIETY OF CHEMISTRY

PAPER

View Article Online
View Journal

Cite this: DOI: 10.1039/d5tb02180d

Combined experimental and DFT studies of amino acid adsorption on biomimetic apatite: application to serine

Youness Hajji, Christophe Drouet, Stéphanie Sarda * and Corinne Lacaze-Dufaure

Biomimetic apatite nanocrystals, as synthetic analogs of bone apatite, offer a more realistic bone mineral model than regular stoichiometric hydroxyapatite (HAP) for studying biomolecule–bone mineral interactions. This is due to the presence, on the constitutive nanocrystals of bone apatite and biomimetic counterparts, of a hydrated ionic surface layer that closely mimics the bone mineral surface. In the present work, a relevant model of the biomimetic apatites in solution, in particular focusing on their very peculiar interface structuration, is proposed using first-principles calculations. Moreover, the adsorption of a model amino acid relevant to biomineralization, namely serine, on synthetic biomimetic apatite is addressed under aqueous conditions using a combined experimental and first-principles computational approach. Experimentally, adsorption isotherms were established at a physiological pH and were compared to the literature data, and the release of calcium and phosphate ions in solution upon serine adsorption was monitored for the first time to better understand the underlying sorption mechanism. Adsorption data fitted well with the Freundlich model, and calculated parameters showed a low adsorbed amount as well as a low affinity for the surface of the apatite substrate. The results indicate that serine adsorbs onto the apatite surface without significantly disturbing the ionic environment. Second, density functional theory (DFT) simulations, using an explicit water solvent model, revealed several energetically favorable adsorption configurations. In these configurations, the serine molecule interacts with the non-apatitic hydrated surface layer through electrostatic interactions involving (COO^-/Ca^{2+}) and (NH_3^+/HPO_4^{2-}) ions. The water molecules at the water/biomimetic apatite interface also play a role in the serine adsorption. Computed interatomic distances and Bader charge analysis confirmed that the adsorption is predominantly governed by electrostatic forces and hydrogen bonding, with no charge transfer. This study points to the relevance of such an integrative experimental/computational approach when dealing with complex surface structures as in bone(-like) apatites, to enhance our understanding of the interaction between biomimetic apatite surfaces and biomolecules such as the amino acid serine.

Received 25th September 2025,
Accepted 9th February 2026

DOI: 10.1039/d5tb02180d

rsc.li/materials-b

1. Introduction

The inorganic phase of bone and dentin, and other mineralized tissues, is composed of nonstoichiometric, nanocrystalline apatite (calcium phosphate phase).[1] Biomimetic apatites can be prepared under close-to-physiological conditions, and are now widely recognized as a reference system for studying the reactivity of bone-like apatite with various circulating species such as ions, (bio)molecules or drugs. This is due to their chemical composition and structural properties being similar to those of native bone apatite, as well as excellent intrinsic biocompatibility.[2–5] Interest in apatite materials has grown significantly since the 1980s, and even more obviously so since the development of methods to prepare biomimetic analogs, significantly more reactive than high-temperature/stoichiometric phases such as hydroxyapatite (HAP) or β-tricalcium phosphate. This has been driven by the demonstrated relevance of these materials in various fields[6] such as nanotechnologies,[7] biomineralization,[8–10] drug delivery systems,[11,12] bone tissue engineering[13,14] and bio-separations,[15] among others.

The adsorption of proteins or drugs onto calcium phosphate apatites plays a crucial role in both mineralized tissues and apatite-based synthetic biomaterials.[16–18] Several bone-specific proteins, such as osteocalcin and osteopontin, as well as more generic biomolecules such as albumin and phospholipids, have

Univ. Toulouse, CNRS, Toulouse INP, CIRIMAT, Toulouse, France.
E-mail: stephanie.sarda@iut-tlse3.fr

been shown to strongly adsorb onto apatite surfaces.[19–24] These adsorption processes are believed to regulate apatite nucleation, crystal growth, and dissolution *in vivo*.[20–23] In the context of biomaterials, the interaction between (bio)molecules/drugs and calcium phosphate surfaces is thought to influence key biological processes such as cell recruitment and differentiation, thereby playing a major role in implant biointegration and bioactivity.[25] For example, a strong correlation has been demonstrated between the biological activity of bone-adsorbing molecules such as bisphosphonates which are commonly used in bone disease treatments (*e.g.* for osteoporosis) and their adsorption properties on apatitic substrates.[24,26,27] Several experimental studies have also emphasized the importance of investigating the adsorption behavior on apatitic substrates using simple model molecules such as individual amino acids (*e.g.*, serine,[28,29] phosphoserine,[28–30] glycine,[31,32] lysine[33] and leucine[33,34]). Serine, as illustrated in Fig. 1 in its zwitterionic form present at physiological pH, is one of the most abundant amino acids in proteins, and thus represents a relevant simple model molecule.[35] Studying its adsorption on biomimetic apatite can contribute to a better understanding of molecular-level processes involved in biomolecule–apatite interactions, of prime relevance to biomineralization.

From a computational point of view, numerous studies over the past two decades have investigated the interaction between biomolecules and stoichiometric hydroxyapatite (HAP) surfaces using both first-principles methods[36–39] and classical molecular dynamics simulations.[40–43] These studies have examined a variety of systems, including small biomolecules and larger peptides modeled in either the gas phase or aqueous environments. These theoretical works[29,32,37,39,42,44,45] provided valuable insights into biomolecule–HAP interactions, showing that adsorption behavior is influenced by the chemical reactivity of both the surface substrate and the adsorbed species. These investigations revealed that adsorbates can adsorb in either neutral or ionic forms depending on HAP surface termination. For instance, glycine was found to adsorb either in its zwitterionic form or in an anionic form, thus involving proton transfer to a surface phosphate group on HAP surfaces.[36] Additionally, it was also demonstrated that specific functional groups, such as NH_3^+, COO^-, and $O–PO_3^{2-}$, could play a critical role in the interactions of molecules with HAP surfaces through electrostatic binding with the calcium and phosphate ions present on the HAP surface.

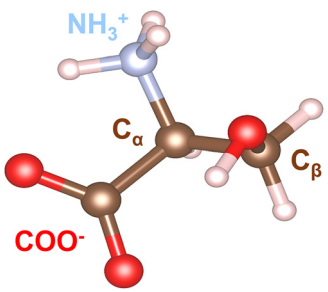

Fig. 1 Zwitterionic molecular structure of serine (COO^-/NH_3^+). Atoms are color-coded as follows: carbon (brown), oxygen (red), nitrogen (blue), and hydrogen (white).

However, all of these studies were performed on stoichiometric hydroxyapatite. While they provided valuable general insights, they overlooked the complex surface chemistry of biological apatites. Indeed, bone apatite and its synthetic biomimetic analogues exhibit various specificities compared to HAP. In addition to nonstoichiometric and nanocrystalline characteristics (with typically plate-like nanocrystals elongated along the *c*-axis), they present a very peculiar surface state consisting of a ''non-apatitic'' hydrated and ionic surface layer that covers a (nonstoichiometric) apatitic core. This non-apatitic surface layer is not present on stoichiometric HAP crystals and has been experimentally evidenced by several techniques such as FTIR[2,3,5] and solid-state NMR.[46] This reactive surface layer, rich in labile ionic species (*i.e.* easily exchangeable when in solution), plays a critical role in governing the key role of bone mineral in bone homeostasis, and is thought to constrain the interaction mechanisms at the biomolecule–mineral interface. To better reflect bone conditions, improve the understanding of molecular-level mechanisms involved in the biomineralization process, and further develop drug-loaded biomaterials, it is necessary to deepen the general understanding of this hydrated layer and its interaction with circulating molecules. Investigating adsorption phenomena is a key prerequisite in this regard, and numerical models of biomimetic apatite surfaces are well-suited for this purpose.

For the first time, a relevant atomic scale model of biomimetic apatites, in particular focusing on their very peculiar surface structuration, was recently proposed in our previous work using first-principles calculations under vacuum.[47] This model was validated by comparing our calculated data under vacuum to a set of experimental results, including the FTIR vibrational features of a synthesized freeze-dried biomimetic apatite. The synthetic biomimetic apatite that we used was matured for one day, mimicking freshly precipitated bone mineral, without carbonation to limit the degree of complexity while remaining representative of hydrated apatites. The synthesis was carried out at room temperature, and therefore far below the boiling point of water, to obtain a biomimetic sub-stoichiometric apatite with a hydrated ionic layer on the surface. This layer can be seen as an incomplete transformation of crystallization, involving surface ions whose speciation is close to that found in solution (typically with HPO_4^{2-} ions instead of PO_4^{3-}).

Being now in possession of this first-of-a-kind model which depicts the local ionic organization of the surface of biomimetic apatites analogous to bone mineral in detail, it is relevant to address their interaction with circulating biomolecules or drugs. This will help to better understand biomineralization processes as well as therapeutic biomaterials for bone repair. The present study involved experimental and computational investigations of the adsorption of serine (Ser), a model amino acid relevant to biomineralization, on a reference biomimetic apatite surface, in aqueous solution. Experimentally, a biomimetic apatite sample was synthesized and thoroughly characterized;

then the Ser adsorption isotherm was determined under aqueous conditions at physiological pH, providing direct insight into serine uptake behavior; the results were discussed and compared to the limited literature data. Additionally, calcium and phosphate ion release into the remaining solution after adsorption was monitored to assess changes in the surrounding ionic environment of the substrate, which has never been done before. This allowed better understanding of the underlying adsorption mechanism. In parallel, density functional theory (DFT) calculations were performed to focus on a biomimetic apatite model representative of a biomimetic apatite in aqueous solution and inspired by the model for the freeze-dried biomimetic apatite previously developed and reported.[47] For this purpose, a new model with a water/apatite interface was developed and explicit solvent molecules were included. This model helped us in a second step to identify energetically favorable serine adsorption conformations and to analyze the nature of the interactions at the biomolecule–mineral interface. To the best of our knowledge, the interaction between serine and biomimetic apatite has not yet been thoroughly explored at the atomic scale using first-principles methods. While previous studies have demonstrated that small amino acids can adsorb onto calcium phosphate surfaces,[36–38] the specific mechanisms involved in these interactions, especially in the context of the non-apatitic hydrated ionic layer characteristic of bone(-like) apatite, remain unclear. This study aims to clarify the preferred adsorption sites and orientations, evaluate the adsorption strength, and determine the role of functional groups in stabilizing the molecule on the surface by combining experimental and theoretical approaches.

2. Materials and methods

2.1. Experimental

2.1.1. Preparation of an apatite substrate. In this study, a (non-carbonated) biomimetic apatite was synthesized *via* aqueous precipitation at ambient temperature and physiological pH.[5] An aqueous solution (75 mL) of calcium nitrate tetrahydrate ($Ca(NO_3)_2{\cdot}4H_2O$, 0.3 M, Merck) was added to 150 mL of diammonium hydrogen phosphate aqueous solution ($(NH_4)_2HPO_4$, 0.6 M, VWR) under continuous stirring. After 5 minutes of mixing, the resulting precipitate was allowed to mature in the reaction medium for 24 hours (aging in solution). The gel obtained was then recovered by filtration using a Büchner funnel, thoroughly washed with deionized water, and subsequently freeze-dried. The resulting powder was then sieved (<125 μm) and stored in a freezer until use. The same non-carbonated biomimetic apatite was used in our previous work to obtain a relevant model of biomimetic apatite's structure and in particular its surface structuration under vacuum.[47]

A stoichiometric hydroxyapatite (HAP) sample was used for the purpose of comparison, and was synthesized following the same protocol as the one described in our previous work.[47] Only key characterization data (XRD and FTIR) are shown here for reference purposes.

2.1.2. Physicochemical characterization of the adsorbent. Stoichiometric hydroxyapatite and biomimetic apatite (matured for 1 day) were both characterized by X-ray powder diffraction (XRD). The analysis was carried out using a Bruker D8 diffractometer with monochromatic Cu Kα radiation (λ = 1.5418 Å). Diffraction patterns were recorded in the 2θ range from 20° to 60°, with a step size of 0.02° and a counting time of 1 second per step. The apparent crystallite dimensions were calculated from the (310) and (002) lines by applying Scherrer's formula.[48]

Fourier-transform infrared (FTIR) spectra were recorded with a Thermo Scientific Nicolet iS50 spectrometer in the spectral range of 400 to 4000 cm^{-1} (128 scans, resolution 1 cm^{-1}), using the KBr pellet method. Spectral decomposition was performed in the $\nu_4(PO_4)$ domain, after linear baseline subtraction following the approach of Kauppinen *et al.*[49] The method for biomimetic apatite was specifically adapted from Rey *et al.*[2]

The calcium content of the synthesized solids was determined using atomic absorption spectroscopy (AAS, ICE 3000, Thermo Scientific), while the phosphate content was quantified by UV-vis spectrophotometry based on the phospho–vanado–molybdenic complex method.[50] The determination of the atomic Ca/P ratio was then estimated with a relative error of 1%. The specific surface area of the biomimetic apatite powders was evaluated by nitrogen adsorption using the BET method, on an ASAP 2020 instrument (Micrometrics) (see Fig. S1). Before measurement, the powder was outgassed at 80 °C for 12 hours, with all measurements performed in triplicate to ensure the reproducibility and accuracy of the results.

2.1.3. Serine adsorption experiments. Serine ($HO–CH_2–CH(NH_2)–COOH$, Sigma) was used as an adsorbate in this study. A stock solution of 0.1 M was prepared by dissolving the appropriate amount in a potassium chloride aqueous solution (0.001 M) – KCl being used to maintain a nearly constant ionic force during the sorption study – and working solutions with serine concentrations ranging from 0.1 to 10 mM were freshly prepared from the stock solution. The pH of the solution was subsequently adjusted to approximately 7.4 by the addition of HCl and KOH solutions. For each adsorption experiment, 100 mg of the synthesized biomimetic apatite was dispersed in 5 mL of the serine solution in a polyethylene tube, sonicated for 2 minutes, and incubated for 1 hour at 37 °C. Following the incubation period, the resulting suspensions were centrifuged for 20 min at 5000 rpm. The supernatants were collected by filtering the samples through Millipore membranes with a pore size of 0.2 μm and subsequently analyzed. Control samples, consisting of the adsorption solution incubated without serine, were used as blanks. To ensure the analytical reliability of the results, all adsorption experiments were performed in triplicate.

2.1.4. Solution analysis after adsorption. The quantification of serine in the solution after adsorption was performed using ultra-performance liquid chromatography (UPLC, Waters Acquity) coupled to a single quadrupole detector (SQD, Waters) through electrospray ionization (ESI). This approach enabled the effective separation and sensitive detection of amino

compounds, particularly suitable for low molecular weight analytes such as serine. The chromatographic separation was achieved using a Poroshell 120 HILIC-Z column (2.1 × 100 mm, 2.7 μm), which was operated at 40 °C. A gradient elution was applied using two mobile phases: phase A composed of 90% water and 10% ammonium formate (200 mM, pH 3), and phase B consisting of 90% acetonitrile and 10% ammonium formate (200 mM, pH 3). The flow rate was maintained at 0.8 mL min^{-1}. In these conditions, serine eluted at 4.9 minutes. The mass detector was configured with a capillary voltage of 3 kV and a cone voltage of 30 V. The ion source was maintained at 150 °C, with a desolvation gas temperature of 450 °C and a flow rate of 900 L h^{-1}. The HILIC-based UPLC-ESI-SQD method has been demonstrated to provide a reliable and selective approach for the quantification of serine in solution, offering advantages in terms of sensitivity, reproducibility, and compatibility with complex matrices. The equilibrium concentrations were determined from peak intensities using a standard calibration curve, ranging from 0 to 10 mmol L^{-1}. To ensure the reliability of the analytical process, all measurements were performed in triplicate.

The amount of serine adsorbed, Q_{ads} (mol g^{-1}), was then calculated using the following equation:

$$Q_{ads} = \frac{V(C_0 - C_{eq})}{W} \quad (2.1)$$

where V is the volume of the solution (L), C_0 and C_{eq} are the initial and equilibrium concentrations of serine, respectively (mol L^{-1}), and W is the mass of apatite used (g).

The phosphate concentration in the solution after adsorption was measured by UV-vis spectrophotometry, a method based on the formation of the phospho–vanado–molybdenic acid complex.[50] The calcium content in solution was determined using atomic absorption spectroscopy (AAS).

2.2. Computational details

2.2.1. Structural models

2.2.1.1. Liquid water. A model was constructed using 87 water molecules placed in an orthorhombic simulation box with dimensions a = 9.438 Å, b = 20.000 Å, and c = 13.726 Å, yielding a density close to 1.00 g cm^{-3}, consistent with the experimental density of liquid water at room temperature. The a and c dimensions were selected to correspond to those of the biomimetic apatite model in order to enable subsequent modeling of the mineral/water interface. The system was submitted to *ab initio* molecular dynamics (AIMD, see Fig. S2) for 30 ps and at an average temperature of 300 K, using a Nosé–Hoover thermostat,[51–53] with a time step of 1 fs. A representative configuration extracted from the equilibration phase was used to build the solid/liquid water interface in biomimetic apatite model for investigating later serine adsorption.

2.2.1.2. Biomimetic apatite/water model and serine adsorption. Inspired by the model developed in our recently-published work,[47] a simulation box with dimensions of 9.438 Å, 42.000 Å, and 13.726 Å along the a, b, and c axes, respectively, was used for the calculations. The dimensions of this slab may not reflect realistic lateral surface heterogeneity. However, using a larger slab to locally break the surface homogeneity would have been too much computationally expensive (AIMD + static DFT optimizations). This supercell was sufficiently large in the three directions to ensure the convergence of the wave function at the Gamma point and to minimize interactions between the adsorbed molecule and its periodic images. To complement this slab model, a representative configuration was extracted from the equilibration phase of bulk liquid water and added on top of the slab to simulate liquid water on the biomimetic apatite model. This initial configuration was used as the starting geometry for *ab initio* molecular dynamics (AIMD) simulations (NVT simulation of 10 ps) to allow sufficient equilibration of the water layer at the interface (Fig. S3) with the atoms of the biomimetic apatite model kept fixed, while only the water molecules allowed to move. The temperature was maintained at 300 K using a Nosé–Hoover thermostat,[51–53] with a time step of 1 fs. Following the equilibration, a snapshot configuration was extracted and subsequently optimized using DFT. This optimized geometry was then employed as the model system for studying the adsorption of serine.

The serine molecule was introduced in its zwitterionic form (NH_3^+–$CH(CH_2OH)$–COO^-), which is predominant at physiological pH. It was manually positioned above the hydrated ionic layer of the biomimetic apatite surface at a distance of approximately 2.5–3.0 Å, allowing potential interactions with surface Ca^{2+} and HPO_4^{2-} ions. Three distinct adsorption configurations, including liquid water as previously described, were built to allow different interaction modes between the molecule and the surface. In the first configuration, the carboxylate group was oriented towards the surface; in the second configuration, the ammonium group was the closest interacting moiety and in the last configuration, both the carboxylate and hydroxyl groups were then positioned so as to be involved in the interaction. These initial geometries were subjected to AIMD simulations (NVT ensemble at an average temperature of 500 K, 6 ps run for each initial geometry) to allow structural sampling of adsorption configurations. Representative snapshots from each simulation were subsequently optimized using DFT.

2.3. Calculations

2.3.1. DFT calculation settings. In the present study, all DFT calculations were performed with the periodic plane-wave basis set code VASP (Vienna ab initio Simulation Package).[54–57] All reported results were obtained with the projector augmented wave (PAW) method.[58,59] The generalized gradient approximation proposed by Perdew, Burke, and Ernzerhof (PBE) was employed to estimate the exchange–correlation energy.[60] In addition to the standard PBE functional, Grimme's approach was used to account for dispersion energy (DFT-D3 (BJ)) with Becke–Johnson damping.[61,62] The plane-wave cutoff was set to 700 eV, the valence electrons were $1s^1$ for hydrogen, $3s^23p^3$ for phosphorus, $3s^23p^64s^2$ for calcium, $2s^22p^4$ for oxygen, $2s^22p^2$ for carbon (C) and $2s^22p^3$ for nitrogen. The electronic convergence criterion was fixed at a value less than 10^{-6} eV and

atomic positions were optimized until all atomic forces became lower than 10^{-2} eV Å^{-1}. Centered *k*-point grids were used for *k*-point sampling at the Gamma point.

All structural visualizations and figures presented in this work were prepared using the VESTA software package.[63]

2.3.2. Adsorption energy calculation. The adsorption energies were calculated by subtracting the total energy of the system in which the molecule is positioned 10 Å away from the surface in the aqueous phase (referred to as the "unbonded" state) from the total energy of the system with the molecule (serine) adsorbed on the surface (referred to as the "bonded" state). In this context, the adsorption energy can be calculated by the following equation:

$$E_{ads} = E_{serine/bonded} - E_{serine/unbonded} \quad (2.2)$$

2.3.3. Bader charge calculation. Bader charge analysis[64] was performed on the fully relaxed configurations. For each atom within the serine molecule, Bader charges were evaluated both before and after adsorption. The charge transfer between the molecule and the apatite surface was then calculated:

$$\Delta Q_{serine} = Q_{serine/bonded} - Q_{serine/unbonded} \quad (2.3)$$

where $Q_{serine/bonded}$ is the total Bader charge of the adsorbed serine molecule, and $Q_{serine/unbonded}$ is the total Bader charge of the serine molecule without interaction with the apatite surface. The value of ΔQ_{serine} reflects the electronic charge transfer associated with the adsorption process.

2.3.4. Radial distribution function. Radial distribution functions (RDFs) were computed to characterize the structural organization of bulk liquid water (20 ps of the equilibrated part of the trajectory used for RDFs generation) and of the water film on biomimetic apatite surfaces (using 6 ps of the equilibrated part of the trajectory). For these systems, a custom Python script that processed atomic coordinates was used. RDF pairs were calculated to evaluate structural differences between bulk and interfacial environments. The RDF $g(r)$ was computed using the following expression:

$$g(r) = \frac{N(r)}{\rho \times V_{shell}(r)} \quad (2.4)$$

where $N(r)$ is the number of atomic pairs, ρ refers to the average density of particles, and $V_{shell}(r)$ is the volume of the spherical shell at radius r, adjusted to account for partial truncation at the slab boundaries. Periodic boundary conditions were applied and interatomic distances were calculated using the minimum image convention. The shell volumes were corrected based on the vertical position of each reference atom to avoid including contributions outside the defined slab.

For serine, RDFs were computed from static optimized conformations to quantify the interatomic distances between specific functional groups in the serine molecule (COO^-, NH_3^+, and OH) and ionic species of the biomimetic apatite model (Ca^{2+} and HPO_4^{2-}). These RDFs were used to identify preferred interaction distances, and were not normalized by density since they represent individual conformational snapshots rather than time-averaged distributions.

3. Results and discussion

As previously mentioned, understanding serine adsorption on biomimetic apatite surfaces under realistic physiological conditions is expected to gain significantly from an integrated approach combining both experimental and theoretical analyses. In the first part of this section, the experimental results will be presented. Detailed physicochemical characterization of the synthesized biomimetic apatite nanocrystals (matured for 1 day) was conducted using different characterization techniques including XRD, FTIR spectroscopy and specific surface area measurements. Following this, Ser adsorption experiments were performed in aqueous media, and the results were analyzed using isotherm models. The release of calcium and phosphate ions was also monitored to assess whether the adsorption process affects the mineral composition in solution and thus the mechanism of adsorption.

In the second part, the theoretical investigations will be described. Using DFT-based calculations, Ser adsorption was studied at the atomic scale on a structurally/chemically realistic biomimetic apatite model. To this end, the model will include an apatitic core, a hydrated ionic surface layer, and an explicit layer of liquid water. A series of energetically favorable adsorption configurations will be optimized, and their interaction features will be analyzed through interatomic distances and Bader charge analysis.

3.1. Experimental results

3.1.1. Adsorbent characteristics. The results of the physicochemical analyses (XRD and FTIR) of the apatite used in this study for the adsorption of serine are illustrated in Fig. 2. The synthesized biomimetic apatite analysis displays a low Ca/P ratio of 1.35 ± 0.01, characteristic of a calcium-deficient apatite as in bone and in accordance with previous results.[27,28] The specific surface area was determined to be 167.2 ± 0.4 m^2 g^{-1} (Fig. S1). This value is consistent with the findings documented in the literature regarding poorly-crystallized apatites that resemble bone mineral.[12,28]

The powder obtained exhibited XRD patterns (Fig. 2(a)) characteristic of poorly crystalline apatitic calcium phosphates compared to well-crystallized stoichiometric HAP.[5] Crystallite dimensions were estimated to approximately 251 nm in length and 45 nm in width using Scherrer's equation applied to the (002) and (310) diffraction peaks, respectively. These values confirm the expected nanocrystalline nature of the sample, which was precipitated under close-to-physiological conditions (room temperature, pH ≈ 7.4, no thermal drying). These dimensions are comparable to those of biological apatites as in bone mineral,[65] thereby further substantiating the significance of the synthesized material as a biomimetic model. Fourier Transform Infrared (FTIR) spectroscopy is a particular useful technique for providing complementary information on

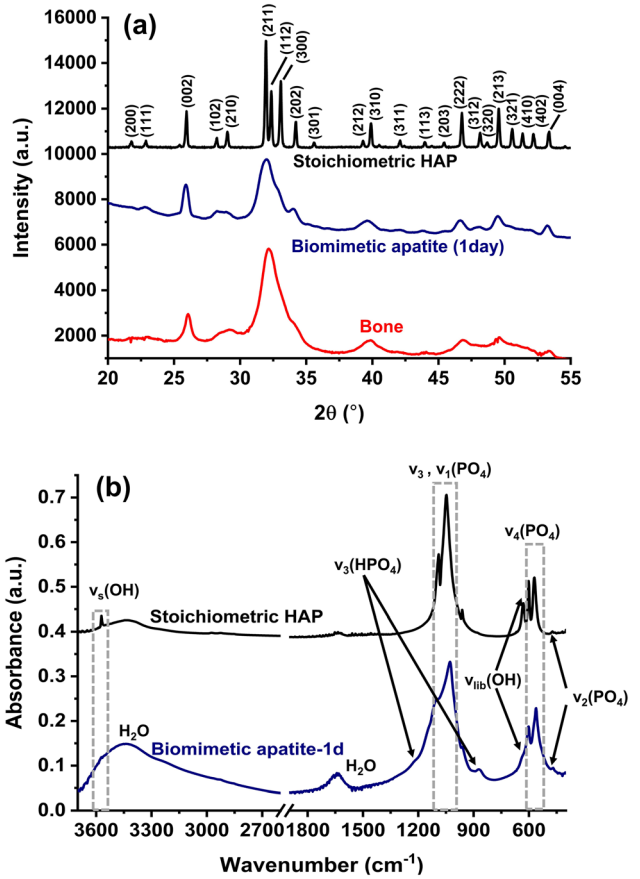

Fig. 2 (a) XRD patterns of the synthesized biomimetic apatite maturated 1 day used in this work, as well as a stoichiometric hydroxyapatite (HAP)[47] and a natural bone sample (rat bone, 9 months old, CIRIMAT internal collection); (b) FTIR spectra for the biomimetic apatite and the stoichiometric HAP in spectral range of 3600–450 cm^{-1}.

the local chemical environments of phosphate groups and, to some extent, hydroxide ions in the apatite structure.[5] The FTIR spectrum of the biomimetic apatite matured for one day, used in this study, displays characteristic vibration bands of a bone-like apatite, compared to the FTIR spectrum of a stoichiometric hydroxyapatite reference (HAP),[5] as illustrated in Fig. 2(b). In particular, the presence of apatitic PO_4 vibration bands at 469 (ν_2), 561–603 (ν_4), 960 (ν_1) and 1000–1103 cm^{-1} (ν_3) may be observed. In addition, low intensity bands related to apatitic OH^- ions at 3560 and 632 cm^{-1}, as well as shoulders observed around 872 and 1145 cm^{-1} attributed to HPO_4^{2-} ions (ν_3), are also evident. The presence of weak bands OH^- and the presence of HPO_4^{2-} bands highlight the non-stoichiometric nature of the synthesized powder, further confirming its biomimetic character, in contrast to well-crystallized stoichiometric HAP, which lacks these spectral features.

More vibrational spectral details are shown in Fig. 3(a) and (b). These figures illustrated the spectral decomposition in the $\nu_4(PO_4)$ domain for the biomimetic apatite and the HAP reference, respectively, which evidences vibration bands assigned to the presence of apatitic and non-apatitic PO_4 and HPO_4 environments. The computed frequencies, based on spectral decomposition are reported in Table S1 for both biomimetic apatite and HAP. The vibrational response of biomimetic apatites differs significantly from that of well-crystallized HAP, particularly in this spectral domain: in addition to the characteristic apatitic PO_4^{3-} vibrational bands at around 603, 575, and 561 cm^{-1}, a band is observed around 550 cm^{-1} associated with HPO_4^{2-} groups in apatitic environments. Other bands are attributed to non apatitic ionic environments: at 534 cm^{-1} corresponding to non-apatitic HPO_4^{2-} and a band near 617 cm^{-1} generally assigned to non-apatitic PO_4^{3-}. A libration band (corresponding to the vibration of the O–H dipole in its local site) of apatitic OH^- ions is also typically detected around 632 cm^{-1}, as previously mentioned. These additional features do not correspond to ions occupying regular lattice sites within the HAP structure; rather, they emerge from ions positioned at or near the surface of the nanocrystals, present in the non-apatitic hydrated ionic surface layer, as documented in numerous studies over the past two decades.[2–5]

From a physicochemical perspective, nanocrystalline biomimetic apatites as those prepared in the present work thus

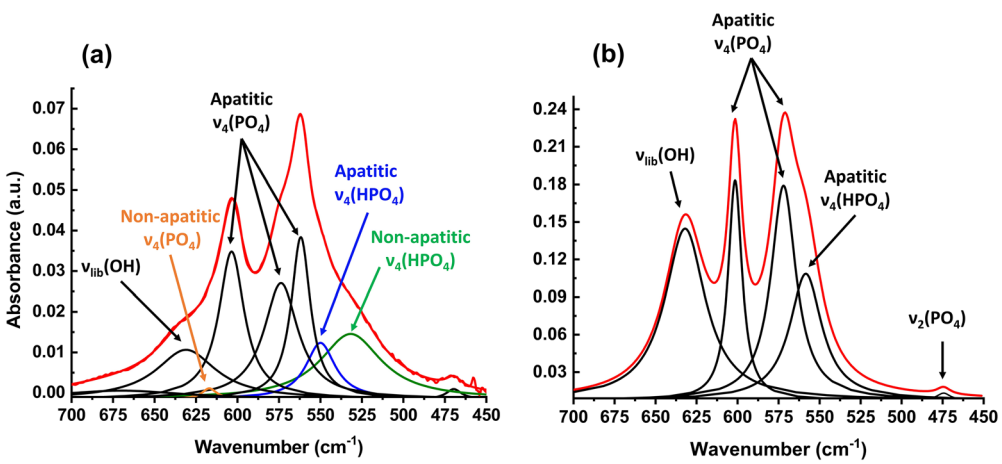

Fig. 3 Spectral decomposition in the $\nu_4(PO_4)$ domain for the biomimetic apatite (a) and the HAP reference (b).

exhibit specific features that distinguish them clearly from stoichiometric hydroxyapatite (HAP), and reflect their closer resemblance to biological apatite. All in all, several specificities can be demonstrated here including (i) the nanoscale crystal size, (ii) the nonstoichiometric global composition and (iii) the presence of a non-apatitic hydrated ionic layer and water molecules.

3.1.2. Analysis of solutions after adsorption. As demonstrated in prior kinetic studies, the adsorption equilibrium for serine onto synthetic apatite substrates is typically reached rapidly, within 10 to 15 minutes.[28] Thus, the adsorption experiments reported in the present study were conducted within an incubation time of one hour to ensure complete adsorption. These experiments were conducted within the physiological pH value (~7.4) and at room temperature, over an initial serine concentration range of 0.20 to 10 mM (see Table 1 for details).

The results of the adsorption experiments show that the adsorbed amount of serine increases with its solution concentration without reaching saturation in the tested range. Fig. 4(a) presents the adsorption isotherm obtained at physiological pH (~7.4) and 37 °C for a 1-hour incubation period, *i.e.* the evolution of the amount of serine adsorbed Q_{ads} (μmol m^{-2}) on the synthesized biomimetic apatite from dilute aqueous solutions (0–8 mM) as a function of the equilibrium concentration in solution C_{eq} (mmol L^{-1}) after adsorption experiments. Upon mathematical modeling, the experimental isotherm was found to follow a Freundlich-type behavior with a good correlation coefficient (r^2 = 0.98) and a low root mean square error (RMSE = 0.019 μmol m^{-2}), indicating a gradual and continuous uptake. The Freundlich model is described by the following equation:

$$Q_{ads} = K_F \times C_{eq}^{m} \quad (3.1)$$

where Q_{ads} is the amount adsorbed (μmol m^{-2}), C_{eq} is the equilibrium concentration (mmol L^{-1}), and K_F (μmol m^{-2}) and m are Freundlich constants, which corresponds to the adsorption constant affinity and capacity, respectively.[28] These results are in agreement with the previous study by Benaziz *et al.*,[28] which examined the adsorption of serine on another bone-inspired apatite substrate, also suggesting a Freundlich-type mechanism. In adsorption experiments of biomolecules or drugs onto apatitic supports showing a small amount adsorbed, the isotherm can indeed often be well described by the Freundlich model, as evidenced by the glycine molecule.[31] Such molecules weakly interact with apatite surfaces due to their functional groups which display only low affinity for the surface of the apatite, such as carboxylate for example. Such an adsorption model is characteristic of the presence of non-equivalent adsorption sites (heterogeneous surface sites). However, when biomolecules exhibit high affinity for the apatite surface and may reach significantly larger adsorbed amounts in similar concentration ranges, the adsorption isotherms generally follow a Langmuir-type behavior. Such an adsorption model is then considered to display equivalent adsorption sites, and no interaction among adsorbed species, up to the formation of a monolayer on the apatitic surface.[66] This is the case of phosphoserine[28] or bisphosphonate molecules,[27] which were reported to exhibit phosphate or phosphonate groups, respectively. Such adsorption mechanisms are then generally accompanied by a plateau in the quantity adsorbed at saturation. In some instance, it may be associated with a simultaneous ion exchange process between the biomolecules in solution and some phosphate (or carbonate) ions present on the surface of the apatitic substrate.

From the fit of the isotherm of adsorption of serine (Fig. 2(a)), the adsorption parameters K_F and m were calculated (see Table 2): the adsorption affinity constant K_F was found to reach 0.065 ± 0.009 μmol m^{-2}, and the Freundlich exponent parameter m was 0.96 ± 0.08. These results confirm the adequacy of the Freundlich model. These Freundlich parameters are close to those previously reported by Benaziz *et al.*[28] for serine adsorbed on bone-inspired apatite (K_F = 0.058 μmol m^{-2}, m = 0.87). A comparison of the adsorption of glycine on stoichiometric HAP (K_F = 0.046 μmol m^{-2}, m = 0.84),[37] and serine reveals a higher affinity for the apatitic surface and a higher adsorbed amount on biomimetic apatite. In the present study, serine exhibits a close-to-linear isotherm trend (m closer to 1), suggesting a homogeneous adsorption process without any saturation under the tested conditions. These differences are likely influenced by the nature of the apatite surface used in each study (biomimetic apatite *vs.* stoichiometric HAP) and the functional groups exhibited by each amino acid tested (Table 2).

Fig. 4(b) shows the variations in phosphate and calcium concentrations in the remaining solution after adsorption as a function of the amount of serine adsorbed. The amount of calcium and phosphate were found to remain low and stable throughout the adsorption process. This phenomenon can be attributed to a small dissolution of the apatite, as is characteristic of any ionic crystal system. This finding suggests that serine adsorption occurs without significant ion exchange between the solution and the surface of the substrate, which is consistent with the Freundlich model. These results suggest that serine adsorbs through low-energy interactions with surface ions of the apatite, likely involving hydrogen bonding or electrostatic interactions with surface groups of the apatite, rather than through mechanisms that would disrupt the mineral structure such as ion exchanges.

Table 1 Experimental data of adsorption of serine on the synthetized biomimetic apatite (matured for 1 day) at physiological pH (~7.4) and 1 hour at 37 °C: initial concentration (C_0) in mmol L^{-1}, equilibrium concentration (C_{eq}) in mmol L^{-1}, and amount adsorbed (Q_{ads}) in μmol m^{-2}

Serine		
C_0 (mmol L^{-1})	C_{eq} (mmol L^{-1})	Q_{ads} (μmol m^{-2})
0.200	0.134 ± 0.020	0.020 ± 0.006
0.400	0.300 ± 0.016	0.029 ± 0.004
0.600	0.474 ± 0.022	0.037 ± 0.006
1.000	0.856 ± 0.039	0.042 ± 0.012
1.500	1.246 ± 0.015	0.075 ± 0.005
2.000	1.697 ± 0.017	0.088 ± 0.005
4.000	3.259 ± 0.104	0.192 ± 0.003
6.000	4.537 ± 0.624	0.320 ± 0.039
8.000	6.727 ± 0.136	0.382 ± 0.028

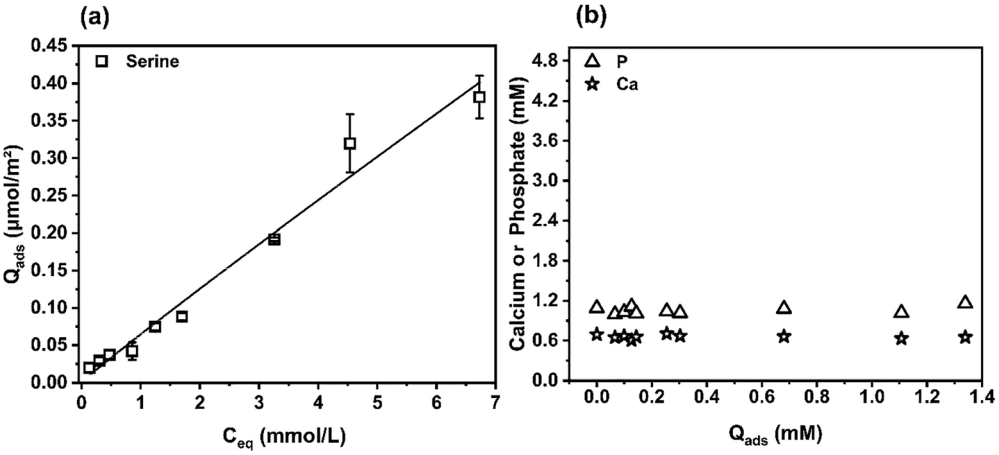

Fig. 4 (a) Adsorption isotherm of serine at physiological pH (~7.4), incubated for 1 hour and at 37 °C onto biomimetic apatite (matured for 1 day); (b) variation of phosphate and calcium concentrations in solution as a function of the adsorbed amount of serine.

Table 2 Freundlich adsorption parameters of serine onto biomimetic apatite matured for 1 day at physiological pH (~7.4), incubated for 1 hour and at 37 °C (present study):

Freundlich parameters (serine)		
Present study	K_F (µmol m^{-2})	m
	0.065 ± 0.009	0.96 ± 0.08
Other reported studies		
Serine[a 28]	0.058	0.87
Glycine[b 31]	0.046	0.84

[a] Biomimetic apatite maturated 1 day. [b] Stoichiometric hydroxyapatite.

However, in certain instances, another type of mechanism of adsorption was observed on apatitic support, as for tranexamic acid (TAX) adsorption on HAP. As previously published,[67] TAX adsorption isotherm cannot be described by either a Langmuir model or Freundlich one. No adsorption plateau was observed, as the adsorbed amount increased continuously and non-linearly. The concentration of calcium and phosphate ions in solution remained low and stable during the adsorption process, therefore ion exchange during the adsorption process can be excluded. Despite the low binding affinity of TAX for the surface of HA crystals, due to the presence of only a carboxyl and an amino group, which are known to have a relatively low affinity for the surface of apatite, as for serine, significantly high quantities of adsorbed TAX are observed. The adsorption data can be fitted with a Langmuir–Freundlich equation, also referred to as Sips. The Langmuir–Freundlich theory is based on the existence of surface heterogeneities with non-equivalent sites and/or of non-negligible interactions between adsorbed species. As only functional groups which present low affinity for the surface of the apatite, are present on the TAX molecule, the high adsorbed amounts observed suggested a strong interaction between adsorbed molecules, resulting in the probable formation of multilayers of adsorbed molecules, interacting with each other through respectively their COO^- and NH_3^+ terminal groups. The chemical structure of TAX exhibits a high degree of similarity to that of the serine, with the presence of identical functional groups; however, these groups are separated by a carbon ring in the case of TAX, a configuration more rigid than the C–C bonding observed in serine. These differences in chemical structures and chains' mobility could explain the variation in adsorption mechanisms and the low quantity adsorbed in the case of serine, attributable to the potential formation of a monolayer.

To further investigate the interaction mechanism of serine with the biomimetic apatite surface, a computational DFT analysis was performed, with the aim to compute serine adsorption energies for various configurations to identify the functional groups involved in the interaction (*e.g.*, COO^-, $NH_3^+N_3$ and OH).

3.2. Computational results

Based on both our experimental findings and DFT calculations, the underlying mechanism was investigated, as detailed in the subsequent sections.

Before investigating the adsorption behavior of serine, it is essential to present in detail the methodology used to create the biomimetic apatite model in this study. Originally developed in our recent previous work, this model was adapted here to explore molecular adsorption processes.[47] The model was specifically designed to closely replicate the structural and chemical characteristics of biomimetic apatite, similar to (non-carbonated) bone mineral. The model involves three key components: (i) an apatitic crystalline core, representing the ordered phase of an apatitic phase; (ii) a non-apatitic hydrated surface layer, containing bivalent HPO_4^{2-} and Ca^{2+} ions, as well as associated water molecules; and (iii) a outer layer of explicit water molecules reproducing a fully hydrated environment, thus the dynamic interactions occurring at the solid–liquid interface. Taking into account these components is essential to accurately mimic the physicochemical behavior of bone-like apatite and to provide a realistic framework for simulating biomolecular adsorption under aqueous conditions. Further details regarding the model construction, surface preparation, ionic composition, and solvation strategy are provided in the following section.

3.2.1. Bulk liquid water model. *Ab initio* molecular dynamics (AIMD) simulations of liquid water have demonstrated a strong dependence on the choice of the exchange–correlation functional.[68] While GGA-based functionals such as PBE are widely used due to their computational efficiency, they often provide a limited degree of accuracy in describing the structural and dynamical properties of liquid water. This phenomenon is mainly due to their incapacity to effectively capture long-range dispersion interactions and the presence of self-interaction errors, which result in the well-documented over-structuring of water molecules observed in PBE-based simulations.[69–71] The inclusion of empirical dispersion corrections, such as Grimme's D3 scheme, significantly improves the structural description of water and enhances the reliability of simulations involving aqueous systems.[72–76] In the present study, the PBE-D3(BJ) functional is employed. As a first step, bulk liquid water was simulated and radial distribution functions (RDFs) were computed. The details of the simulation cell, the RDF analysis, and the comparison with neutron scattering data can be found in the SI (Fig. S4). The computed RDFs showed good agreement with experimental data,[77] though with slightly enhanced peak intensities indicative of mild overstructuring (a common feature in DFT-based water models). The resulting equilibrated water configuration was then used to construct the hydrated biomimetic apatite/water model, thereby ensuring a realistic representation of interfacial solvation.

3.2.2. Biomimetic apatite/water model. A number of prior studies, based on classical molecular dynamics, have focused on the interaction between stoichiometric HAP and water molecules.[32,78,79] These works demonstrated that the HAP surface is hydrated by a large number of water molecules, leading to the formation of multiple well-structured hydration layers as water remains confined on the HAP surface. The present study investigates for the first time the interactions between a biomimetic apatite model and water.

As previously explained, the water/apatite model was built starting from a conformation taken from the AIMD trajectory (after the equilibration phase) that was optimized using DFT. Fig. 5(a) shows the optimized model that includes an apatitic core, a hydrated ionic layer, and an explicit water layer on the surface.

Fig. 5(b) illustrates the planar-averaged water density as a function of distance from the surface. The density profile (dashed line) was obtained by averaging the water density at intervals of 0.1 Å along the axis from the interface biomimetic apatite/water model. Oscillations in the density are observed. The film can be divided into five distinct layers, as illustrated in Fig. 5(b). These layers are defined by the minima in the density profile. Beyond layer 5, the density gradually decreases to zero, close to the water/vacuum interface, consistent with previous studies of the liquid water/vacuum boundary.[71,80]

The analysis of radial distribution functions (RDFs) provides insights into local atomic arrangements and intermolecular correlations. The O–O (Fig. 5(c)) and H–H (Fig. 5(d)) RDFs for each layer within the water film are then compared to those of bulk liquid water (shaded line). Overall, the computed RDFs for layers 1 to 5 are close to those of bulk water, suggesting that the local structural organization of water molecules is largely maintained throughout the film, even if a mild over-structuring of water near the surface is observed, $g_{O\text{–}O}(r)$ and $g_{H\text{–}H}(r)$ being slightly different for those found in the bulk liquid water, likely due to confinement effects and strong ion–dipole interactions.

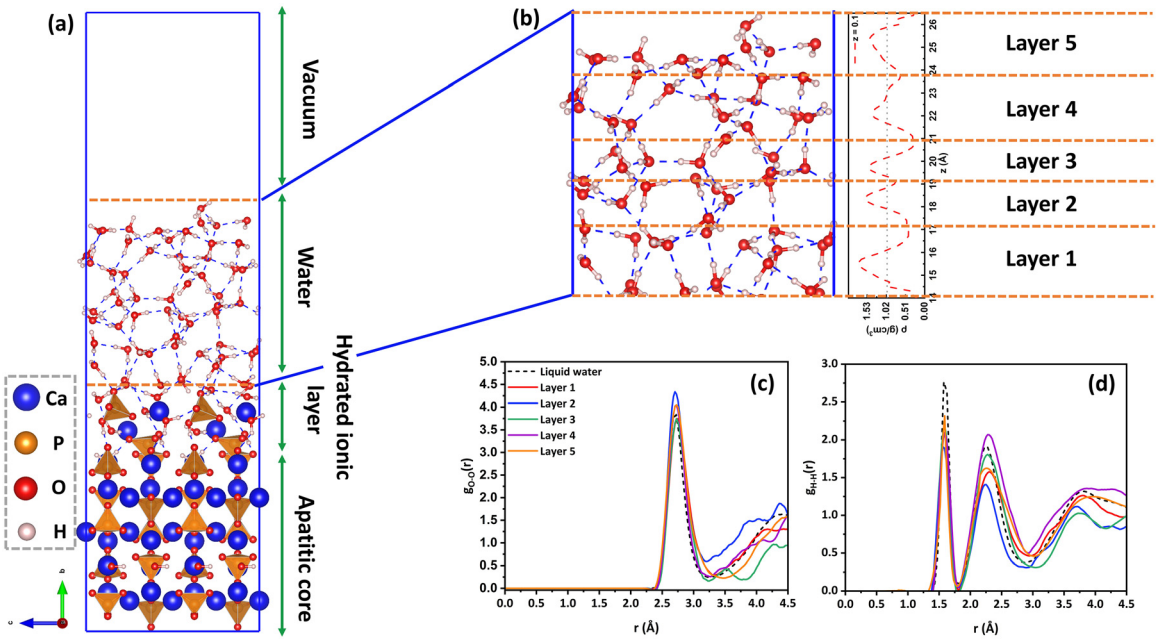

Fig. 5 (a) Optimized biomimetic apatite model obtained from the AIMD, containing an apatitic core, an hydrated ionic layer and an explicit liquid water on the surface; (b) planar-averaged water density obtained by averaging the water density every 0.1 Å (dotted line), along the *z* axis; (c) and (d) oxygen–oxygen and hydrogen–hydrogen radial distribution functions for each layer within the water film on the biomimetic apatite model.

A discussion of the limitations of the water/biomimetic apatite model proposed is necessary. For instance, the surface chemistry composition (HPO_4^{2-}/Ca^{2+} ratio) may not correspond exactly to that ofexperimental nanoparticles in aqueous solution as ions of the hydrated ionic layer of the apatite are labile and there is thus an equilibrium at the water/apatite surface. However, to the best of our knowledge an exact experimental composition cannot be determined. In the present work, a model for computations of the water/apatite interface was proposed, based on the model of the freeze-dried apatite previously validated thanks to comparison between simulated/experimental FTIR spectra.[47]

The following section focuses on the investigation of the interaction of the apatite/water model with a serine molecule.

3.2.3. Adsorption of serine. The present study of the adsorption of the serine molecule on the apatite surface was performed with a surface coverage of θ_{cal} = 7.7 × 10^{-3} molecule $Å^{-2}$ employed for the DFT calculations. As shown in the previous section, the experimental findings reported that the Freundlich model adequately described the adsorption isotherms. Subsequently, even for the largest amount adsorbed of serine (Q_{ads}), saturation was not attained. This ruled out the determination of the experimental coverage at saturation that could be directly compared to the coverage used for computations. However, in order to verify that the computed surface coverage could relate meaningfully to the experimental conditions, the surface coverage corresponding to the largest amount adsorbed of serine (Q_{ads} = 0.382 μmol m^{-2}) was estimated to a value of θ_{exp} = 2.30 × 10^{-3} molecule $Å^{-2}$, which is of the same order as the value used for calculations.

Among the various adsorption geometries studied, the three most stable configurations (Conf. 1–3 that lies within an energy variation of 0.52 eV) are presented in Fig. 6 to illustrate the diversity of the conformations of the system when the serine molecule interacts with the biomimetic apatite surface, in the presence of water molecules. Their relative energies are given in Table 3. Other (less stable) configurations are provided in the SI section (Fig. S5 and Table S2). As shown in Fig. 6, and further detailed in Tables 3 and 4, the adsorbed serine molecule adopts its zwitterionic form (COO^-/NH_3^+) in all configurations. This has been deduced from the values of the inter- and intra-atomic distances and the net charge calculated for each functional group (see Table 4). The variations in the charges of each functional group remain small when comparing the unbonded system and the adsorbed conformations (Conf. 1–3). Even the most pronounced deviation, observed for the COO^- group, does not exceed +0.10 *e*.

Table 3 Computed relative energies (ΔE_{rel} in eV), adsorption energies (E_{ads} in eV) and electronic and dispersion components, and total charge variation on the serine molecule (ΔQ_{ser} in *e*) upon adsorption for the three most stable conformations

Conf.	ΔE_{rel} (eV)	E_{ads} (eV)	E_{ads}^{elec} (eV)	E_{ads}^{disp} (eV)	ΔQ_{ser} (*e*)
Conf. 1	0.000	−0.918	−0.876	−0.042	0.00
Conf. 2	0.175	−0.744	−0.737	−0.007	0.03
Conf. 3	0.517	−0.401	−0.535	0.134	−0.01

Table 4 Functional group charges for the unbonded system and the most stable configurations ($\Delta E_{rel} \leq$ 0.52 eV)

Group	Unbonded system	Conf. 1	Conf. 2	Conf. 3
COO^-	−0.78	−0.73	−0.81	−0.85
NH_3^+	0.38	0.38	0.42	0.39
OH^-	−0.51	−0.52	−0.54	−0.53

In these three configurations, different functional groups of serine interact with the ionic species present in the non-apatitic hydrated ionic layer of the biomimetic apatite model, specifically, the carboxylate (COO^-), amino (NH_3^+), and hydroxyl (OH) groups. To further characterize geometrically these interactions, radial distribution functions (RDFs) were computed for the DFT-optimized structures. The RDFs were calculated for all relevant atomic pairs within 4.5 Å, including $Ca^{2+}/O(COO^-)$, $NH_3^+/O(HPO_4^{2-})$, $OH(H)/O(HPO_4^{2-})$, and $OH(O)/Ca^{2+}$ (Fig. 7 and Fig. S6). These functions provide insight into the local coordination environment. In addition, Table 3 presents the computed energies (ΔE) relatively to the most stable configuration, adsorption energies (E_{ads}), including their electronic and dispersion components, as well as the total charge variation on the serine molecule (ΔQ_{ser}^{tot}) upon adsorption for each conformation.

In the first configuration (Conf. 1), the adsorbed serine molecule adopts a "flat-lying" orientation. In this configuration,

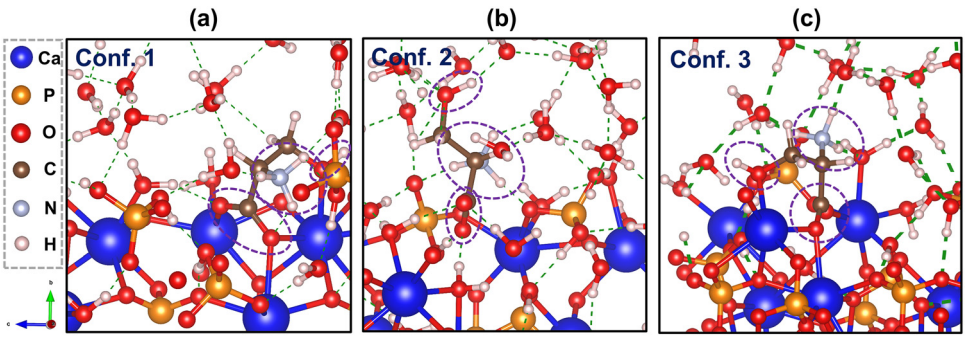

Fig. 6 Optimized adsorbed configurations of serine on the biomimetic apatite surface in presence of water: Conf. 1 (a), Conf. 2 (b) and Conf. 3 (c). Purple dashed lines indicate the serine functional groups (COO^-, NH_3^+, and OH) involved in the interactions with the surface.

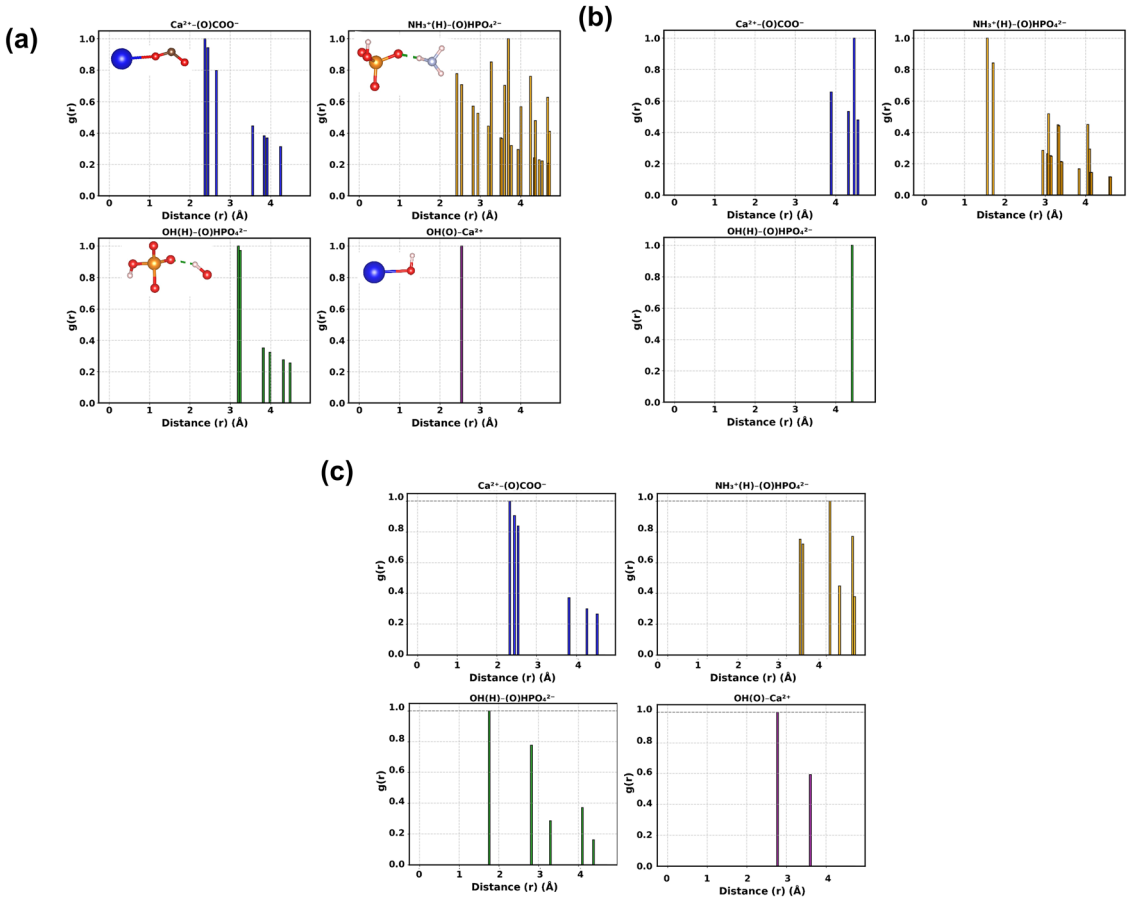

Fig. 7 Computed radial distribution functions (RDFs) for key interatomic interactions : Ca^{2+}/O(COO^{-}), NH_3^{+}/O(HPO_4^{2-}), OH(H)/O(HPO_4^{2-}), and OH(O)/Ca^{2+} for Conf. 1 (a), Conf. 2 (b) and Conf. 3(c).

the carboxylate group COO^{-} is in interaction simultaneously with several surface calcium ions (computed RDFs, Fig. 7(a)). The shortest Ca···O distances are in the range from 2.38 Å to 2.65 Å, indicating strong electrostatic binding. These values are consistent with those reported in the literature for Ca···O interactions, which supports the reliability of our results.[38] The amino group (NH_3^{+}) forms hydrogen bonds with both a hydrogen phosphate group (HPO_4^{2-}) within the hydrated ionic layer of the biomimetic apatite model and nearby interfacial water molecules, with H···O distances of around 2.42 Å. The hydroxyl side chain also contributes to the overall stabilization: the oxygen atom of the OH group coordinates to a surface calcium ion with a Ca···O distance of approximately 2.54 Å, while the hydrogen atom is engaged in hydrogen bonding with a nearby water molecule. The computed adsorption energy for this most stable conformation (E_{ads} = −0.918 eV) indicates a favorable interaction. No substantial charge transfer (ΔQ_{ser} = 0.00e) is observed in this case, which confirms that the adsorption of serine is primarily governed by electrostatic interactions and hydrogen bonding, with stabilization provided by dispersion forces (E_{ads}^{disp} = −0.041 eV representing 4.6% of the adsorption energy).

In the second configuration (Conf. 2), as illustrated in Fig. 6(b), the adsorbed serine molecule adopts a perpendicular orientation relatively to the non-apatitic hydrated ionic layer, interacting predominantly with surrounding water molecules. According to the radial RDFs shown in Fig. 7(b), the carboxylate group is not directly in interaction with calcium ions, with interatomic distances exceeding 3.8 Å. In contrast, the amino group (NH_3^{+}) is engaged in hydrogen bonding with HPO_4^{2-} ions present within the hydrated ionic layer. The shortest hydrogen bonds between NH_3^{+} and HPO_4^{2-} range from 1.57 Å to 1.72 Å. Nevertheless, the NH_3^{+} group exhibits limited interaction with the hydrogen atom of HPO_4^{2-}, with distances typically greater than 4 Å. This adsorption configuration is less stable, with a total relative energy of ΔE_{rel} = 0.175, compared to the first configuration (Conf. 1). The computed adsorption energy in this case (E_{ads} = −0.744 eV) still indicates a favorable interaction of the serine molecule with the surface of the biomimetic apatite model, although it is weaker than in Conf. 1. No substantial charge transfer (ΔQ_{ser} = 0.03e) is observed as in the case of Conf. 1.

The third configuration (Conf. 3), as illustrated in Fig. 6(c), is quite similar geometrically to the Conf.1 with a flat lying molecule positioned on the non-apatitic hydrated ionic layer. This adsorption configuration possesses a total relative energy of ΔE_{rel} = 0.517 eV, in comparison to the first configuration (Conf. 1). The computed adsorption energy in this case (E_{ads} = −0.401 eV) shows a favorable interaction of the serine molecule

with the surface of the biomimetic apatite model, with no substantial charge transfer ($\Delta Q_{ser} = -0.01e$).

These results are in good qualitative agreement with our experimental observations, which demonstrated that serine adsorption followed a Freundlich-type isotherm. Such a behavior is indicative of weak binding between the molecule and the surface, which is typically associated with physisorption mechanisms, as evidenced by the computed adsorption energies and Bader charge analysis. The results of this study suggest the presence of surface sites with varying affinities and moderate binding strength. As shown in Table 3, the electronic component dominates the adsorption energy across all configurations, compared to the dispersion (van der Waals) contribution. However, the dispersion interactions also play a role in stabilizing the adsorbed serine molecules on the biomimetic apatite surface.

These computational outcomes thus facilitate a more precise understanding of the most probable orientation of the serine amino acid molecule when exposed in solution to the surface of bone-like biomimetic apatite. Both experimental and modeling results evidence a relatively low affinity of the serine molecules for such apatite substrates. Beyond the specific case of serine sorption, one can highlight the relevance of combining experiments and DFT calculations to explore more deeply the molecule–mineral mode of interaction. This is a subject of particular relevance to the fields of biomineralization and biomaterials developments.

4. Conclusions

In conclusion, the adsorption of a key amino acid, serine, onto biomimetic apatite under aqueous conditions was investigated for the first time through a combination of experimental measurements and first-principles calculations based on DFT. Experimentally, the serine adsorption isotherm confirmed a detectable molecular uptake under aqueous conditions, although associated with a rather low affinity, well described by the Freundlich model. These results suggest a low and heterogeneous sorption capacity of biomimetic apatite for this amino acid. The monitoring of calcium and phosphate ion concentration release in solution revealed no significant variation with the amount of adsorbed serine, indicating that the serine adsorption process did not involve ion release or uptake from the solution.

In addition, DFT calculations revealed that serine was adsorbed in its zwitterionic form, with the carboxylate (COO^-) group coordinating to surface calcium ions, while the protonated amine (NH_3^+) group forms hydrogen bonds with surface phosphate groups and interfacial water molecules. The hydroxyl side chain further contributes to stabilization through both electrostatic interactions and hydrogen bonding. In contrast to the findings of numerous preceding investigation conducted on stoichiometric hydroxyapatite in gas-phase or simplified aqueous models, the present study highlights the specific role of the non-apatitic hydrated ionic layer, which is characteristic of biomimetic apatite. The surface environment significantly influences the interaction mechanisms. Bader charge analysis and radial distribution functions confirmed that serine adsorption was primarily governed by non-covalent interactions with no charge transfer. These theoretical results are consistent with the weak affinity of the serine observed experimentally with the biomimetic apatite surface.

By incrementing our recently published model of biomimetic apatite under vacuum and its surface state, the present manuscript evidences the correlation between experimental hypotheses on the mechanism of adsorption of serine and a structural study of the surface of the apatite substrate at the atomic scale. This work demonstrates the importance of considering the local atomic organization at the surface of biomimetic apatites in the adsorption behavior of serine as a model amino acid relevant to biomineralization. These findings contribute to a deeper understanding of amino acid interactions with bone-like apatite materials and provide molecular-level insights that may be relevant to biomineralization and the design of bioactive surfaces. Above all, the study also showed how the reported model of the hydrated layer of bone-like apatites could be used to explore the interaction with molecular species of applicative and fundamental interest. In this view, this work opens the way to other upcoming studies, including with other amino acids or peptidic moieties exhibiting other functional end groups and thus more complex adsorption mechanisms (*e.g.*, ion exchange process…), with the view to enhance molecular affinity for bone-like apatite surfaces. Furthermore, this dual experimental/computational approach could be extended to other fields of application involving molecular/substrate interfaces such as in biomedical engineering, catalysis, archeological sciences, depollution and beyond.

In particular, one of the perspectives of this work is the examination of the various forms of known carbonates that are present in biological apatites. The explicit integration of these different forms of carbonates ions, which are currently absent from the models, will allow to obtain a more accurate representation of the actual chemical composition of the bone mineral and to better model apatitic carbonate biomaterials that exhibit greater resorbability *in vivo*. Furthermore, it will be necessary to introduce into future atomic-scale model ions of biological interest such as Na^+, Mg^{2+} or even Sr^{2+}, frequently detected in biological apatites and which participate in the structuration and reactivity of the hydrated ionic layer. The objective of this study will thus be to further explore the chemical and ionic complexity inherent to natural bone mineral.

Author contributions

Youness Hajji: conceptualization, methodology, software, investigation, formal analysis, data curation, visualization, writing original draft, writing – review & editing. Christophe Drouet: conceptualization, methodology, investigation, formal analysis, data curation, validation, supervision, project administration, writing – original draft, writing – review & editing.

Stéphanie Sarda: conceptualization, methodology, investigation, formal analysis, data curation, validation, supervision, project administration, funding acquisition, writing – original draft, writing – review & editing. Corinne Lacaze-Dufaure: conceptualization, methodology, software, investigation, formal analysis, data curation, validation, supervision, project administration, funding acquisition, writing – original draft, writing – review & editing.

Conflicts of interest

There are no conflicts to declare.

Data availability

The data supporting this article have been included as part of the supplementary information (SI). Supplementary information is available. See DOI: https://doi.org/10.1039/d5tb02180d.

Acknowledgements

This work was granted access to the HPC resources of CALMIP supercomputing centre under the allocation [p22029] and to the HPC resources from GENCI-IDRIS under the allocation [AD010813856]. It was also supported by the French Ministry of Higher Education and Research [Y. H., PhD grant]. We are grateful to Isabelle Fabing for scientific and technical expertise on UPLC provided by the Integrated Screening Platform of Toulouse (PICT, IBiSA).

References

1 H.-R. Wenk and F. Heidelbach, *Bone*, 1999, **24**, 361–369.
2 C. Rey, M. Shimizu, B. Collins and M. J. Glimcher, *Calcif. Tissue Int.*, 1990, **46**, 384–394.
3 C. Rey, C. Combes, C. Drouet, H. Sfihi and A. Barroug, *Mater. Sci. Eng., C*, 2007, **27**, 198–205.
4 C. Rey, C. Combes, C. Drouet and M. J. Glimcher, *Osteoporosis Int.*, 2009, **20**, 1013–1021.
5 N. Vandecandelaere, C. Rey and C. Drouet, *J. Mater. Sci.: Mater. Med.*, 2012, **23**, 2593–2606.
6 J. J. Gray, *Curr. Opin. Struct. Biol.*, 2004, **14**, 110–115.
7 T. Vo-Dinh, *Nanotechnology in biology and medicine: methods, devices, and applications*, CRC Press, 2007.
8 L. L. Hench, R. J. Splinter, W. C. Allen and T. K. Greenlee, *J. Biomed. Mater. Res.*, 1971, **5**, 117–141.
9 M. J. Glimcher, L. C. Bonar, M. D. Grynpas, W. J. Landis and A. H. Roufosse, *J. Cryst. Grow.*, 1981, **53**, 100–119.
10 J. Song, V. Malathong and C. R. Bertozzi, *J. Am. Chem. Soc.*, 2005, **127**, 3366–3372.
11 B. Palazzo, M. Iafisco, M. Laforgia, N. Margiotta, G. Natile, C. L. Bianchi, D. Walsh, S. Mann and N. Roveri, *Adv. Funct. Mater.*, 2007, **17**, 2180–2188.
12 A. Bouladjine, A. Al-Kattan, P. Dufour and C. Drouet, *Langmuir*, 2009, **25**, 12256–12265.
13 N. Hijón, M. V. Cabañas, I. Izquierdo-Barba and M. Vallet-Regí, *Chem. Mater.*, 2004, **16**, 1451–1455.
14 A. P. Tomsia, E. Saiz, J. Song and C. R. Bertozzi, *Adv. Eng. Mater.*, 2005, **7**, 999–1004.
15 E. Schröder, T. Jönsson and L. Poole, *Anal. Biochem.*, 2003, **313**, 176–178.
16 T. Matsumoto, M. Okazaki, M. Inoue, S. Yamaguchi, T. Kusunose, T. Toyonaga, Y. Hamada and J. Takahashi, *Biomaterials*, 2004, **25**, 3807–3812.
17 C. J. Wilson, R. E. Clegg, D. I. Leavesley and M. J. Pearcy, *Tissue Eng.*, 2005, **11**, 1–18.
18 J. E. Davies, *Anat. Rec.*, 1996, **245**, 426–445.
19 A. L. Boskey, W. Ullrich, L. Spevak and H. Gilder, *Calcif. Tissue Int.*, 1996, **58**, 45–51.
20 P. V. Hauschka and F. H. Wians, *Anat. Rec.*, 1989, **224**, 180–188.
21 R. W. Romberg, P. G. Werness, B. L. Riggs and K. G. Mann, *Biochemistry*, 1986, **25**, 1176–1180.
22 H. A. Goldberg, K. J. Warner, M. C. Li and G. K. Hunter, *Connect. Tissue Res.*, 2001, **42**, 25–37.
23 C. Robinson, S. J. Brookes, J. Kirkham, W. A. Bonass and R. C. Shore, *Adv. Dent. Res.*, 1996, **10**, 173–180.
24 A. Jung, S. Bisaz and H. Fleisch, *Calcif. Tissue Res.*, 1973, **11**, 269–280.
25 V. Hlady and J. Buijs, *Curr. Opin. Biotechnol*, 1996, **7**, 72–77.
26 I. Cukrowski, L. Popović, W. Barnard, S. O. Paul, P. H. van Rooyen and D. C. Liles, *Bone*, 2007, **41**, 668–678.
27 P. Pascaud, P. Gras, Y. Coppel, C. Rey and S. Sarda, *Langmuir*, 2013, **29**, 2224–2232.
28 L. Benaziz, A. Barroug, A. Legrouri, C. Rey and A. Lebugle, *J. Colloid Interface Sci.*, 2001, **238**, 48–53.
29 R. Mathew, B. Stevensson, M. Pujari-Palmer, C. S. Wood, P. R. A. Chivers, C. D. Spicer, H. Autefage, M. M. Stevens, H. Engqvist and M. Edén, *Chem. Mater.*, 2022, **34**, 8815–8830.
30 D. N. Misra, *J. Colloid Interface Sci.*, 1997, **194**, 249–255.
31 A. Barroug, C. Rey, M. Fauran, J. Trombe, G. Montel and G. Bonel, *Bull. Soc. Chim. Fr.*, 1985, 535–539.
32 H. Pan, J. Tao, X. Xu and R. Tang, *Langmuir*, 2007, **23**, 8972–8981.
33 A. El Rhilassi, M. Mourabet, H. El Boujaady, M. Bennani-Ziatni, R. El Hamri and A. Taitai, *Appl. Surf. Sci.*, 2012, **259**, 376–384.
34 A. El Rhilassi, M. Mourabet, H. El Boujaady, H. Ramdane, M. Bennani-Ziatni, R. El Hamri and A. Taitai, *J. Mater. Environ. Sci.*, 2012, **3**, 515–524.
35 L. Wang, Q. Liang, Z. Wang, J. Xu, Y. Liu and H. Ma, *Food Chem.*, 2014, **148**, 410–414.
36 A. Rimola, M. Corno, C. M. Zicovich-Wilson and P. Ugliengo, *J. Am. Chem. Soc.*, 2008, **130**, 16181–16183.
37 N. Almora-Barrios, K. F. Austen and N. H. De Leeuw, *Langmuir*, 2009, **25**, 5018–5025.
38 A. Rimola, M. Corno, J. Garza and P. Ugliengo, *Philos. Trans. R. Soc., A*, 2012, **370**, 1478–1498.
39 A. Rimola, Y. Sakhno, L. Bertinetti, M. Lelli, G. Martra and P. Ugliengo, *J. Phys. Chem. Lett.*, 2011, **2**, 1390–1394.

40 N. H. De Leeuw and J. A. L. Rabone, *CrystEngComm*, 2007, **9**, 1178–1186.
41 J.-W. Shen, T. Wu, Q. Wang and H.-H. Pan, *Biomaterials*, 2008, **29**, 513–532.
42 N. Almora Barrios, PhD thesis, UCL (University College London), 2010.
43 Q. Wang, M. Wang, K. Wang, Y. Liu, H. Zhang, X. Lu and X. Zhang, *Biomed. Mater.*, 2015, **10**, 032001.
44 Z. Xu, Y. Yang, Z. Wang, D. Mkhonto, C. Shang, Z.-P. Liu, Q. Cui and N. Sahai, *J. Comput. Chem.*, 2014, **35**, 70–81.
45 Z. Lou, Q. Zeng, X. Chu, F. Yang, D. He, M. Yang, M. Xiang, X. Zhang and H. Fan, *Appl. Surf. Sci.*, 2012, **258**, 4911–4916.
46 C. Jäger, T. Welzel, W. Meyer-Zaika and M. Epple, *Magn. Reson. Chem.*, 2006, **44**, 573–580.
47 Y. Hajji, C. Drouet, S. Sarda, O. Marsan and C. Lacaze-Dufaure, *Surf. Interfaces*, 2025, **62**, 106176.
48 P. Scherrer, *Nachr. Ges. Wiss. Goettingen*, 1918, **2**, 8–100.
49 J. K. Kauppinen, D. J. Moffatt, H. H. Mantsch and D. G. Cameron, *Appl. Spectrosc.*, 1981, **35**, 271–276.
50 G. Charlot, *Chimie analytique quantitative*, Masson, 1974.
51 S. Nosé, *J. Chem. Phys.*, 1984, **81**, 511–519.
52 N. Shuichi, *Prog. Theor. Phys. Suppl.*, 1991, **103**, 1–46.
53 W. G. Hoover, *Phys. Rev. A: At., Mol., Opt. Phys.*, 1985, **31**, 1695–1697.
54 G. Sun, J. Kürti, P. Rajczy, M. Kertesz, J. Hafner and G. Kresse, *J. Mol. Struct. THEOCHEM*, 2003, **624**, 37–45.
55 G. Kresse and J. Hafner, *Phys. Rev. B: Condens. Matter Mater. Phys.*, 1993, **47**, 558–561.
56 G. Kresse and J. Furthmüller, *Comput. Mater. Sci.*, 1996, **6**, 15–50.
57 G. Kresse and J. Furthmüller, *Phys. Rev. B: Condens. Matter Mater. Phys.*, 1996, **54**, 11169.
58 D. Vanderbilt, *Phys. Rev. B: Condens. Matter Mater. Phys.*, 1990, **41**, 7892–7895.
59 G. Kresse and J. Hafner, *J. Phys.: Condens. Matter*, 1994, **6**, 8245.
60 J. P. Perdew, K. Burke and M. Ernzerhof, *Phys. Rev. Lett.*, 1996, **77**, 3865–3868.
61 S. Grimme, J. Antony, S. Ehrlich and H. Krieg, *J. Chem. Phys.*, 2010, **132**, 154104.
62 S. Grimme, S. Ehrlich and L. Goerigk, *J. Comput. Chem.*, 2011, **32**, 1456–1465.
63 K. Momma and F. Izumi, *J. Appl. Crystallogr.*, 2011, **44**, 1272–1276.
64 M. Yu and D. R. Trinkle, *J. Chem. Phys.*, 2011, **134**, 064111.
65 P.-Y. Chen, A. G. Stokes and J. McKittrick, *Acta Biomater.*, 2009, **5**, 693–706.
66 I. Langmuir, *J. Am. Chem. Soc.*, 1918, **40**, 1361–1403.
67 S. Sarda, F. Errassifi, O. Marsan, A. Geffre, C. Trumel and C. Drouet, *Mater. Sci. Eng., C*, 2016, **66**, 1–7.
68 M. J. Gillan, D. Alfè and A. Michaelides, *J. Chem. Phys.*, 2016, **144**, 130901.
69 M. V. Fernández-Serra and E. Artacho, *J. Chem. Phys.*, 2004, **121**, 11136–11144.
70 J. VandeVondele, F. Mohamed, M. Krack, J. Hutter, M. Sprik and M. Parrinello, *J. Chem. Phys.*, 2005, **122**, 14515.
71 L.-M. Liu, M. Krack and A. Michaelides, *J. Chem. Phys.*, 2009, **130**, 234702.
72 C. Zhang, J. Wu, G. Galli and F. Gygi, *J. Chem. Theory Comput.*, 2011, **7**, 3054–3061.
73 J. Wang, G. Roman-Perez, J. M. Soler, E. Artacho and M.-V. Fernandez-Serra, *J. Chem. Phys.*, 2011, **134**, 024516.
74 I.-C. Lin, A. P. Seitsonen, M. D. Coutinho-Neto, I. Tavernelli and U. Rothlisberger, *J. Phys. Chem. B*, 2009, **113**, 1127–1131.
75 I.-C. Lin, A. P. Seitsonen, I. Tavernelli and U. Rothlisberger, *J. Chem. Theory Comput.*, 2012, **8**, 3902–3910.
76 S. Sakong, K. Förster-Tonigold and A. Groß, *J. Chem. Phys.*, 2016, **144**, 194701.
77 A. K. Soper, *ISRN Phys. Chem.*, 2013, **2013**, 1–67.
78 D. Zahn and O. Hochrein, *Phys. Chem. Chem. Phys.*, 2003, **5**, 4004–4007.
79 T. T. Pham, T. Lemaire, E. Capiez-Lernout, M. Lewerenz, Q.-D. To, J. K. Christie, D. Di Tommaso, N. H. De Leeuw and S. Naili, *Theor. Chem. Acc.*, 2015, **134**, 59.
80 I.-F. W. Kuo and C. J. Mundy, *Science*, 2004, **303**, 658–660.

